Quantum Dynamical Study of β-Hydrogen Transfer in Two Selected Late-Transition-Metal Complexes

Maik Bittner and Horst Köppel*

Theoretische Chemie, Physikalisch-Chemisches Institut, Universität Heidelberg, Im Neuenheimer Feld 229, 69120 Heidelberg, Germany

Received: June 22, 2004; In Final Form: September 9, 2004

The $[CpM(PH_3)H(C_2H_4)]^+$, (M = Rh, Co), complexes have been investigated with electronic structure and quantum dynamical methods. Stationary points, including transition states, have been found and characterized with various methods and basis sets. The global minimum of the Rh complex is the ethylene structure, but for the Co complex, it is the agostic structure, in agreement with experiment. A one-dimensional reaction-path profile was calculated and used for a wave packet propagation. The time-dependent wave function and the resulting spectrum have been investigated in detail. Thus, we get a first insight into the β-hydrogen transfer process from a quantum dynamical point of view.

1. Introduction

Olefin insertion into an M−H bond and the reverse process, the β-hydrogen elimination, represent elementary reaction steps which are of fundamental importance to many transition-metal-catalyzed processes, such as hydrogenation, hydroformylation, and olefin polymerization, to mention a few. Correspondingly, there has been much theoretical effort toward characterizing the structural parameters and energetics of the intermediate complexes and transition states,[1−8] which complements the large amount of related experimental investigations (see, for example, refs 9−12 and references therein).

Usually, the insertion proceeds in two steps, as indicated schematically in Figure 1:

1. The hydrogen atom starts to migrate from the metal atom, to which it is covalently bound in the olefin−hydride structure at the left of Figure 1, to the ethylene moiety to form the β-agostic structure in the center of Figure 1.

2. A further rearrangement takes place to yield the ethyl complex at the right of Figure 1. Both reaction steps are indicated as equilibrium processes by the arrows in the figure.

In addition to the electronic structure calculations mentioned already, dynamical calculations are also required and have been performed by Senn et al.[13] and Meier et al.[14] on the AIMD (ab initio molecular dynamics) level or, more specifically, by CPMD (Car−Parinello molecular dynamics) simulations. In either case, the electronic structure problem is solved relatively accurately by DFT (density functional theory) methods, but the nuclear dynamics is treated classically only, basically by solving Newton's equations of motion for the relevant (ground) Born−Oppenheimer surface of the system (although the latter is not explicitly constructed by the CPMD method). There seems to exist virtually no single quantal treatment of the nuclear motion for insertion and elimination processes in transition-metal complexes, nor for many other transition-metal reaction steps. As is well-known, such quantal treatments are of importance for describing coherence and tunneling effects, and also the vibrational structure of electronic spectra. Real-time monitoring

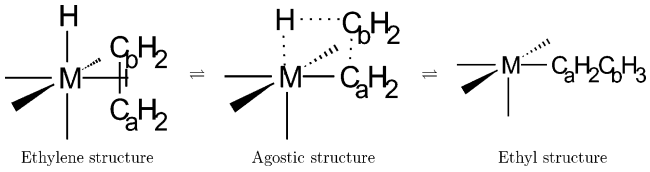

Figure 1. General scheme of the migratory insertion (from left- to right-hand side) and the β-elimination (from right- to left-hand side). M denotes the transition metal.

of bond formation and bond cleavage by femtosecond time-resolved pump−probe spectroscopy[15−17] represents an experimental field which relies on a quantal description of the nuclear motion. It also brings the system into a highly nonequilibrium initial state by the very nature of the short excitation process. The wave packet methodology, which we are going to apply here, is well-established and widely used in the literature for different kinds of systems (see, for example, refs 18−22).

In this paper, we want to perform a first quantal simulation of an insertion/elimination process for a specific transition-metal complex. We focus on late transition metals because here the β-elimination is known to proceed rapidly, which makes this step more easily accessible to a quantal treatment. Also, we rely on a comparison with literature data for related systems, which leads us to choose the title compounds $[CpM(PH_3)H(C_2H_4)]^+$ with M = Rh and Co as model complexes. For the analogous system with M = Ir, structural and energetic data have been provided by Niu et al.,[23] which serve as a natural comparison. Also, for M = Rh and Co, there are experimental data[11] and selected DFT results[3] to compare. The case M = Rh represents the system of interest for the dynamical simulations. To be explicit, the dynamical calculations are performed by wave packet propagation techniques (i.e., the time-dependent Schrödinger equation for nuclear motion is solved numerically). Because of the computational cost, which increases rapidly with increasing number of degrees of freedom, we confine ourselves here to a one-dimensional treatment using the reaction path concept, which is to be considered as the first step toward a more realistic treatment. Nevertheless, this requires as input the full information of the geometric and energetic data of the stationary points of the potential energy surface (PES). Here,

* Corresponding author. Telephone: +49/6221/545214, Fax: +49/6221/545221, E-mail: horst.koeppel@tc.pci.uni-heidelberg.de.

10.1021/jp0472820 CCC: $27.50
Published on Web 11/17/2004

TABLE 1: Nomenclature and Number of Basis Functions of the Modified Basis Sets for the Electronic Structure Calculations

name	size[a]	Rh	P, C, H_{act}[b]	H[b]
split1	178	SDD	6-31G*	[2s][c]
split2	193	SDD	6-31G**	[2s][d]
split3	232	SDD	6-311G**	[2s][e]
split4	217	SDD	6-31G**	[2s, 1p][c]

[a] Number of contracted Gaussian basis functions. [b] H_{act} denotes the active hydrogen atoms (i.e., the migrating hydrogen atom and the ones which are bonded to the terminal ethylenic carbon atom). Those without subscripts denote the others. [c] Exponents and contraction coefficients from the 6-31G** basis set. [d] Exponents and contraction coefficients from the SDD basis set. [e] Exponents and contraction coefficients from the D95 basis set.

we employ DFT methods but estimate their accuracy by comparing with MP2/MP4 and CCSD(T) results. The latter is to be considered an essential part of the present work.

The outline of this article is as follows: Section 2 explains the basic theoretical methods used for this work; Section 3 summarizes the main results. In the latter section, the structural parameters for the investigated transition-metal complexes will be discussed first (Section 3.1), and then we focus on their energetics (Section 3.2). The next subsection, Section 3.3, is devoted to the generation of the potential energy profiles, which are used for the quantum dynamical simulations in Section 3.4. We finish this article with some conclusions and an outlook in Section 4.

2. Theoretical Methods

2.1. Electronic Structure Calculations. Because of the relatively large system size, we focus on DFT[24] methods. Three different density functionals have been employed, BP86,[25,26] BLYP, and B3LYP.[27,28] It was not clear a priori if these methods describe the geometry and energy of such a transition-metal complex accurately. Therefore, we also compare with Møller−Plesset perturbation theory (MP2−MP4)[29−31] and coupled-cluster calculations, where we also included noniterative triple excitations (CCSD(T)).[32−34] These methods have already been applied in the literature to a variety of transition-metal complexes.[1−8]

For the calculations, we used the standard SDD[35] and 6-31G**[36−38] basis sets. Our standard computational approach will be denoted B3LYP/SDD (the B3LYP functional in combination with the SDD basis set). This is to be verified, on one hand, by improving the basis set. Therefore, we combined the SDD basis set on the metal atom with Pople's 6-31G** basis on the other atoms (see Table 1). The result is a basis set, called split4, which has additional d-functions on the phosphorus and carbon atoms and additional p-functions on hydrogen (in comparison with pure SDD). On the other hand, we also want to make a comparison of B3LYP/SDD with accurate CCSD(T) calculations, where we have to make a compromise with the size of the basis set because of the high computational cost of this method. We used two compromise basis sets: one version, called split1, is to abandon the p-functions on the hydrogen atoms by just using the 6-31G basis set there. The other possibility is to treat the reactive or central hydrogen atoms more accurately than the others. This can be accomplished by the basis sets split2 and split3, which have additional p-functions on the active hydrogen atoms but none on the others (SDD). The carbon and phosphorus atoms are treated more accurately in the split3 than in the split4 basis set by using the 6-311G** basis. For a characterization of these four different versions, see Table 1. Within this larger basis set, the carbon atoms have one more sp-function, and phosphorus has six s-functions (rather than one) and five p-functions (rather than three sp-functions) in comparison with the split4 basis. The split1 basis set was used for energy calculations based on MP2/SDD geometrics for the structures, split3 for energy calculations based on B3LYP/split4 geometrics, and split2 for full optimizations with the BP86 density functional. For the electronic structure calculations, the *Gaussian 98* software package[39] was used.

2.2. Generation of Potential Energy Profiles. To calculate the reaction-path energy profile, the intrinsic reaction coordinate (IRC)[40−43] method is used. It calculates a reaction path with respect to a mass-weighted coordinate. The reaction coordinate reflects how much and how many atoms are moving between two points along the curve. (The motion of heavy atoms is weighted more strongly than the same motion of light atoms.) The algorithm needs as an input a transition state (TS) structure. Following the reaction path means solving a differential equation for the IRC *s*.[40−43] A first approximation to the solution of this equation is a series of linear steps. The segment of the reaction path between two adjacent points on the path is approximated by an arc of a circle. The arc is computed so that the gradients of the end points are tangent to the path.

To locate the TS, a combined scanning and transit-guided quasi-Newton (STQN) method[44] is used. STQN uses a linear or quadratic synchronous transit approach to get closer to the quadratic region of the PES around the TS. When this region is reached, the algorithm utilizes a quasi-Newton or eigenvector-following algorithm to complete the optimization. Here, a variant of the STQN method (QST3) is used where a reactant, a product, and an initial guess for the TS are needed as input.

2.3. Wave Packet Propagation. As an essential and novel part of this work (which extends earlier studies of catalytic processes), we investigate the insertion and elimination steps by quantum dynamical simulations. The quantum dynamical calculations rely on a wave packet propagation method where the time-dependent Schrödinger equation for nuclear motion is solved explicitly.[18−22] For the integration of the time-dependent Schrödinger equation, the Lanczos−Arnoldi algorithm (LA)[45,46] is used. Because of the imaginary part of the potential (CAP, see later text), the Hamiltonian is not hermitian. Lanczos−Arnoldi is a generalization of the short iterative Lanczos (SIL) integrator[47] for this case. The reaction-path potential and wave packet are represented on a one-dimensional grid (discrete variable representation, DVR,[48,49] and fast Fourier transformation, FFT[50−52]). The number of grid points chosen is 512 and spans an interval from −500 to 1700 $m_e^{1/2}a_0$ along the IRC.

If a wave packet is propagated on the reaction-path potential as specified in the preceding paragraph, one has to take care of the boundaries of the grid to prevent unphysical reflections and wraparounds. These can be avoided by absorbing the part of the wave function near the boundaries by a complex absorbing potential (CAP).[53−56] Here, a CAP closes the potential on one side. It has the form

$$W(x) = i\eta(x - x_0)^2 \qquad \text{for } x \le x_0 \tag{1}$$

where η is the strength parameter and x_0 is the starting position of the CAP.

The CAP parameters η and x_0 have to be adjusted such that the CAP fulfills two conditions concerning the interaction, namely giving (1) no reflection and (2) no transmission of an incoming wave packet. One can shortly state that stationary solutions (i.e., solutions independent of the parameters) are required. The conditions are usually fulfilled for whole intervals

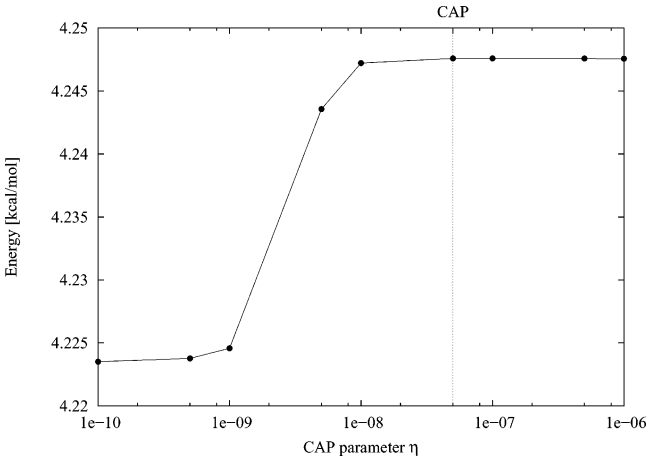

Figure 2. Dependence of the ground-state energy on the CAP parameter η (see eq 1). The value selected for the subsequent calculations is indicated by the dashed vertical line.

of parameters. The middle of the interval has to be found by a scan over the parameter space.

We monitored the energy of the ground state, the lifetime of this state, and the total norm of the wave packet after 24 fs of propagation as a function of the CAP parameters η and x_0. This is shown for the energy in Figure 2. The parameters chosen for the subsequent calculations are $\eta = 5 \times 10^{-8}$ kcal/mol $1/(m_e a_0^2)$ and $x_0 = -131.9\ m_e^{1/2} a_0$. (The latter is the coordinate where the calculated IRC potential ends.) The resulting complex part of the potential is included in Figures 7 and 9 at the left border.

If a wave packet reaches the other side of the reaction-path potential (ethyl minimum see Figure 7 and below), it can form a stable solution there, or if its energy is high enough, it can tunnel through the next barrier and isomerize to another structure. Therefore, we decided to extrapolate the potential on this side by a real harmonic function which has the form

$$V(x) = \mu(x - x_1)^2 \qquad \text{for } x \geq x_1 \tag{2}$$

where μ is the force constant and x_1 is the position of the minimum. We fitted this continuation to be approximately symmetric with respect to the ethyl minimum. The parameters are $\mu = 5 \times 10^{-8}$ kcal/mol $1/(m_e a_0^2)$ and $x_1 = 1262.6\ m_e^{1/2} a_0$. The resulting real part of the potential is included in Figures 7 and 9 at the right border.

The spectra are calculated by an FFT of the autocorrelation function

$$C(t) = \langle \psi_0 |\ \mathrm{e}^{-i\mathscr{H}t} | \psi_0 \rangle \tag{3}$$

of the initial wave packet $|\psi_0\rangle$ and the time-developed one, $\exp(-i\mathscr{H}t)|\psi_0\rangle$. The spectrum is thus given by[57]

$$P(E) = \frac{1}{2\pi} \int \mathrm{d}t\, C(t)\, \mathrm{e}^{iEt}. \tag{4}$$

From the nonhermitian Hamilton operator $\mathscr{H}$, one gets complex energy eigenvalues E. These are extracted with a filter diagonalization scheme[58−61] with a box filter. The real parts give the precise positions of the spectral peaks in the FFT spectrum. These are used to calculate the oscillation frequency of the time-dependent wave function within the potential. The imaginary parts are the lifetimes of the corresponding metastable states. As already mentioned, the lifetime and the energy of the ground state are used to calibrate the CAP.

2.4. Computational Details. The wave packets have been propagated for 4096 fs with time steps of 0.5 fs and a Lanczos order of 30. The starting positions of the initial wave packets are at the first transition state TS1 (0 $m_e^{1/2} a_0$), at the second transition state TS2 (973 $m_e^{1/2} a_0$), and at the agostic structure (96 $m_e^{1/2} a_0$). The widths of these initial wave packets are 17 $m_e^{1/2} a_0$ (TS1 and agostic structure) and 50 $m_e^{1/2} a_0$ (TS2). They were set to the widths of suitable harmonic oscillator ground-state wave functions. The force constants of these harmonic oscillators are defined approximately by the minima of the inverse potentials formed by the energetic barriers at TS1 and TS2. The software used for the wave packet propagation was developed and widely tested for the vinylidene−acetylene isomerization reaction[18] in our group.

3. Results and Discussion

3.1 Structural Parameters of the Stationary Points. First, we obtain the structural parameters of the various stationary points that are of relevance for the insertion/elimination reaction. As already indicated in the Introduction, we have to deal with the ethylene, agostic, and ethyl structures as local minima and the (at least) two transition states TS1 and TS2 interconnecting them. Depending on the details of the system, either the ethylene or the agostic structure represent the global minimum, while for the late transition metals, the ethyl structure is expected to be rather high in energy and separated from the other structures by a low barrier. The theoretical studies of Niu et al.[23] gave these data for the analogous Ir complex, which serves as a natural comparison for the corresponding Rh and Co complexes treated here. Table 2 and Figure 3 summarize the main geometric parameters of the stationary points.

As already described in the Introduction, the insertion is a two-step process (cf. Figures 1 and 3). The two individual steps of the insertion are monitored by two characteristic angles:

1. The migration of the hydrogen atom from the transition metal to the ethylene to form the β-agostic structure is described by the angle $\alpha(C_b{-}M{-}H)$; C_b is the carbon atom to which the migrating H will be attached.

2. The opening of the chain formed by the transition metal and the ethylene/ethyl moiety during the transformation of the agostic to the ethyl structure is described by the angle $\beta(M{-}C_a{-}C_b)$.

The two angles (reaction coordinates) $\alpha(C_b{-}M{-}H)$ and $\beta(M{-}C_a{-}C_b)$ are listed in the last two segments of Table 2. The angle $\alpha(C_b{-}M{-}H)$ decreases from ∼70° in the ethylene structure to ∼30° in the agostic structure, while $\beta(M{-}C_a{-}C_b)$ increases by a small amount from ∼70° to ∼80°.

From the agostic structure, the angle $\beta(M{-}C_a{-}C_b)$ starts to increase from ∼80° (agostic structure) to ∼125° in the ethyl structure, while $\alpha(C_b{-}M{-}H)$ decreases by a small amount of ∼10°. Hence, whereas one angle strongly varies, the other stays approximately constant. The different methods provide similar results for these angles.

For a more detailed inspection, we focus first on the Rh complex. During the insertion, the distance $d(Rh{-}H)$ increases strongly from ∼1.6 Å (strong interaction between Rh and H) to ∼3.4 Å (no interaction). $d(Rh{-}H)$ of ∼1.8 Å corresponds to the agostic structure ($d(Co{-}H)$ is ∼1.7 Å for the Co complex). In the ethylene complex, $d(Rh{-}C_a)$ of ∼2.3 Å corresponds to a moderate bonding of ethylene to the transition metal. During the insertion, one of the carbon atoms (C_a) is bonded to the transition metal, while the other one (C_b) is bent away. This bending is, of course, faster during the second step of the insertion, namely the opening of the chain from the agostic

TABLE 2: Geometric Parameters of the Stationary Points for Different Methods and Basis Sets for the Co, Rh, and Ir Complexes

		ethylene			TS1			agostic			TS2	ethyl		
parameter	method/basis set	Co	Rh	Ir	Co	Rh	Ir	Co	Rh	Ir	Rh	Co	Rh	Ir
d(M−H) [Å]	BLYP/SDD		1.575						1.897				3.484	
	B3LYP/SDD	1.461	1.559		1.475	1.619		1.727	1.871		3.337	3.329	3.461	
	B3LYP/split1		1.566						1.848				3.450	
	B3LYP/split4		1.554			1.607			1.819		3.320		3.444	
	BP86/split2		1.566			1.602			1.778		3.313		3.423	
	B3LYP/mod. DZ[a]			1.585			1.707			1.865				3.244
	MP2/SDD		1.589						1.773				3.432	
d(M−C_a) [Å]	BLYP/SDD		2.261						2.110				2.073	
	B3LYP/SDD	2.132	2.249		2.077	2.165		1.951	2.086		2.086	1.884	2.055	
	B3LYP/split1		2.253						2.090				2.046	
	B3LYP/split4		2.252			2.165			2.093		2.092		2.041	
	BP86/split2		2.220			2.157			2.106		2.093		2.020	
	B3LYP/mod. DZ[a]			2.221			2.140			2.100				2.070
	MP2/SDD		2.176						2.132				2.038	
d(C_b−H) [Å]	BLYP/SDD		2.339						1.196				1.104	
	B3LYP/SDD	2.079	2.306		1.780	1.586		1.182	1.189		1.098	1.096	1.098	
	B3LYP/split1		2.322						1.195				1.100	
	B3LYP/split4		2.314			1.575			1.202		1.096		1.094	
	BP86/split2		2.291			1.555			1.240		1.103		1.102	
	B3LYP/mod. DZ[a]			2.263			1.413			1.220				1.100
	MP2/SDD		2.328						1.246				1.103	
d(C_a−C_b) [Å]	BLYP/SDD		1.425						1.521				1.538	
	B3LYP/SDD	1.401	1.408		1.418	1.443		1.509	1.509		1.533	1.523	1.530	
	B3LYP/split1		1.392						1.491				1.517	
	B3LYP/split4		1.392			1.427			1.487		1.522		1.516	
	BP86/split2		1.411			1.442			1.486		1.525		1.513	
	B3LYP/mod. DZ[a]			1.428			1.477			1.514				1.558
	MP2/SDD		1.464						1.516				1.540	
α(C_b−M−H) [Å]	BLYP/SDD		73						30				18	
	B3LYP/SDD	67	72		56	45		33	30		19	19	18	
	B3LYP/split1		73						30				19	
	B3LYP/split4		73			45			31		19		19	
	BP86/split2		73			44			32		19		19	
	MP2/SDD		75						33				19	
β(M−C_a−C_b) [°]	BLYP/SDD		72						80				126	
	B3LYP/SDD	70	72		72	75		77	80		121	130	125	
	B3LYP/split1		72						80				127	
	B3LYP/split4		73			74			79		121		128	
	BP86/split2		71			74			77		120		130	
	B3LYP/mod. DZ[a]			71			76			80				110
	MP2/SDD		71						76				129	

[a] Data taken from ref 23.

structure to the ethyl complex. When the insertion is completed, the distance of the inner carbon atom is d(Rh−C_a) ≈ 2.1 Å. d(C_b−H) changes, of course, in an opposite way from d(Rh−H). Here, it goes from a large noninteraction distance of ∼2.3 Å to a usual C−H bond length of ∼1.1 Å. d(C_b−H) in the agostic structure is 1.189 Å (B3LYP/SDD). This is ∼8% longer than the C−H distances for the ethylene hydrogens. d(C_a−C_b) is changing from the typical value of ∼1.4 Å in the cationic ethylene structure to a usual single-bond distance of ∼1.5 Å in the ethyl structure.

The different DFT methods and basis sets usually give only small differences in the distances (≤0.03 Å). However, notable exceptions occur (with differences up to 0.09 Å) for the agostic structure. The inclusion of polarization functions is important to describe the geometries accurately. The LANL2DZ basis set is not recommended for this system, because it failed for the agostic structure (and for the transition states as well). Generally, larger deviations occur between DFT and MP2 results for the structural parameters. As a tendency, the MP2 bond lengths are larger for covalent bonds and smaller for others than their DFT counterparts.

Now, we turn briefly to the Co complex. In general, we find that the distances within the Co complex are ∼0.1 Å or more shorter than within the Rh complex. The C_a−C_b distance of the ethylene/ethyl moiety is (of course) for all cases more or less the same. When the migrating hydrogen atom is bonded to ethylene, the distances d(C_b−H) and d(C_a−C_b) are approximately the same for the Co, Rh, and Ir complexes. This result is reasonable, because the influence of the transition metal decreases with the distance from it. A very interesting exception to the shorter distances in the Co complex is d(C_b−H) for TS1. For Co, the C_b−H distance is ∼0.2 Å larger than for the Rh complex. We expect a close relationship to the energetically low-lying TS1 of the Co complex (see text to follow). Concerning the angles, one can say that in the ethylene structure the Co complex is more folded than the Rh complex, while it is more open in the TS1. This does not hold for the ethylene structure. Here, the angular differences are small.

In comparison with the Ir complex,[23] the distances and the angles are not generally larger or smaller than those of the Rh complex. As expected, Co has a stronger influence on the structural parameters than has Ir.

3.2. Energies of the Stationary Points. Table 3 and Figure 4 show the results for the energies of the stationary points for different complexes, correlation methods, and basis sets. The energy of the ethylene structure is always set to zero, and the

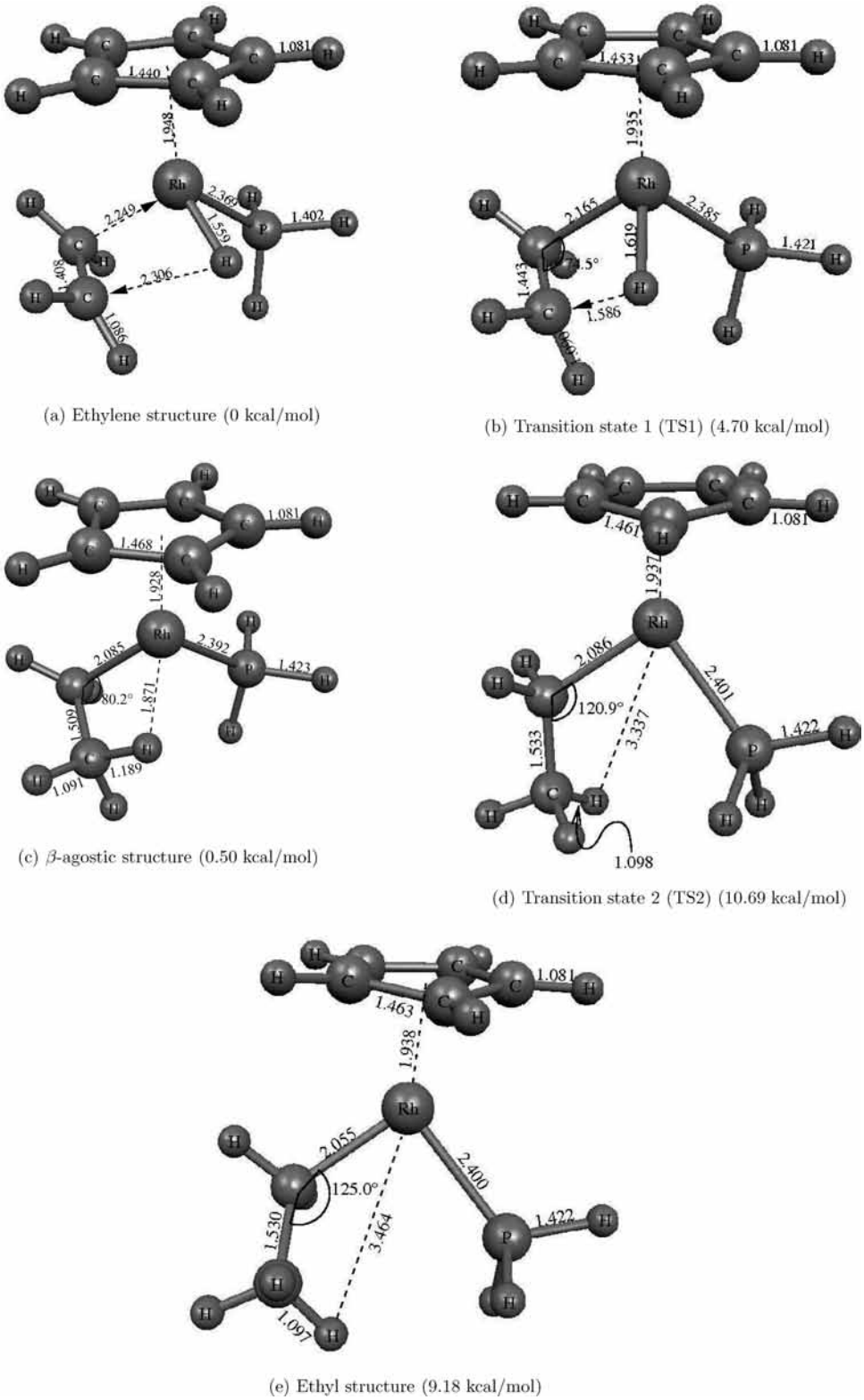

Figure 3. Geometric parameters and energies (B3LYP/SDD) of the various stationary points of relevance to the insertion/elimination process.

other energies are relative to it. First, we focus again on the Rh complex. Figure 4 shows the three minima (ethylene, agostic, and ethyl structure) and two transition states (TS1 and TS2) of the PES, as they are interconnected.

One can divide the calculations of the energies into three groups: DFT, MP2-MP4, and CCSD(T) calculations. Full second-order MP2 optimization has been done for all three minima on the PES (see Tables 2 and 3). On the basis of these geometries, we performed CCSD(T) single-point calculations with the basis set split1. Further MP2-MP4 energy calculations rely on DFT geometrics. On the basis of the B3LYP/split4 geometries, we performed CCSD(T)/split3 single-point calculations (for the nomenclature of the basis sets, see Table 1). This is the highest theoretical quality we obtained; hence, we call that the reference calculation.

Figure 4 gives an overview of the main results, and in Table 3, the theoretical energy data are compiled. The variety of different calculations performed permits us to estimate separately

TABLE 3: Energies of the Stationary Points for Different Methods and Basis Sets for the Co, Rh, and Ir Complexes

M	method/basis set[a]	ethylene[b] [Hartree]	TS1[c] [kcal/mol]	agostic[c] [kcal/mol]	TS2[c] [kcal/mol]	ethyl[c] [kcal/mol]
Co	B3LYP/SDD	−761.42599	0.37	−7.46	∼4.83[d]	3.27
	DFT[e]	0	0.3	−3.4		9.9
Rh	BLYP/SDD	−725.96762		2.08		9.46
	B3LYP/SDD	−726.19314	4.70	0.50	10.69	9.18
	B3LYP/split1	−726.27434		1.42		10.34
	B3LYP/split4	−726.29515	4.64	1.40	12.95	10.95
	BP86/split2	−726.38816	4.17	2.48	16.85	13.88
	CCSD(T)/split3//B3LYP/split4	−724.35826	5.04	3.70	20.67	18.48
	CCSD/split3//B3LYP/split4	−724.28682	5.09	2.97	19.06	17.11
	CCSD/split1//B3LYP/split4	−724.13877		1.82		13.43
	CCSD(T)/split1//MP2/SDD	−724.19457		0.94		12.80
	MP2/SDD//B3LYP/SDD	−723.63734	6.15	5.37	22.89	21.09
	MP3/SDD//B3LYP/SDD	−723.61038	5.05	−1.23	11.71	10.53
	MP4/SDD//B3LYP/SDD	−723.75040	6.71	6.82	23.65	21.71
	MP2/SDD	−723.64632		7.52		23.69
	DFT[e]	0	2.7	−1.0		7.3
Ir	B3LYP/mod. DZ[f]	0	12.91	12.19		17.19
	CCSD/mod. DZ//B3LYP/mod. DZ[f]	0	16.09	15.71		23.41
	DFT[e]	0	6.1	3.7		8.1

[a] Notation: Energy calculation method/basis set//optimization method/basis set. If there is only one method/basis set given, the energy is calculated by a full optimization with the same method. [b] Absolute value of the energy. [c] Energy ΔE relative to the ethylene structure. [d] The energy of TS2 of the Co complex is taken to be the energetic maximum of the scan in Figure 5. [e] Data taken from ref 65. No absolute energies given therein.[f] Data taken from ref 23. No absolute energies given therein.

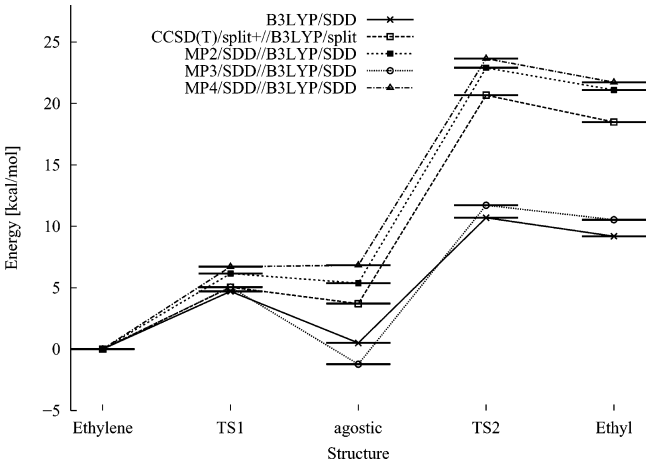

Figure 4. Comparison of different methods (B3LYP, CCSD(T), MP2-MP4), and basis sets (SDD, split3, split4) for the energies of the stationary points for the Rh complex.

the effects of different basis sets and correlation treatments from Table 3. Apparently, the influence of the different basis sets on the B3LYP relative energies is rather small; that is, polarization functions on either P, C, or H atoms are not very important here. The situation is quite different for the coupled-cluster data, where polarization functions on H alone affect the CCSD (and also CCSD(T)) relative energies rather significantly. The effect of disconnected triple (T) excitations, on the other hand, is only minor and allows for significant computational savings by confining oneself to CCSD calculations. Similarly, the change from MP2 to MP4 raises the relative energies of the stationary points by less than 1 kcal/mol. We discard the MP3 data because of the well-known unbalanced weight of the terms in the perturbation expansion,[62] and because it gives the agostic structure as global minimum, which is in clear contrast to the experimental data[9] and all other present theoretical results of Table 3. Comparing DFT, MP2/4, and CCSD/CCSD(T) energies, their agreement is good for TS1, but the difference generally increases for later steps of the insertion process. BLYP and B3LYP agree rather well throughout. On the other hand, the BP86 functional calculation lies much closer to the reference calculation energies than B3LYP. The relative energies of the stationary points of the DFT calculations lie closer to the CCSD-(T)/split1//MP2/SDD calculation than the corresponding MP2/4 data.

TABLE 4: Experimental and Present Theoretical (B3LYP/SDD) Energy Differences between Stationary Points (ΔE in Kcal/Mol)

M	complex		TS2−ethylene	TS2−agostic
Co	$Cp^*M(P(OMe)_3)H(C_2H_4)^+$	expt[a]	6−8 (est.)	11.1
	$CpM(PH_3)H(C_2H_4)^+$	theory[b]	∼4.83	∼12.29
Rh	$Cp^*M(P(OMe)_3)H(C_2H_4)^+$	expt[a]	12.2	
	$Cp^*M(PMe_3)H(C_2H_4)^+$	expt[a]	12.1	
	$CpM(P(OMe)_3)H(C_2H_4)^+$	expt[a]	15.0	
	$CpM(PMe_3)H(C_2H_4)^+$	expt[a]	15.0	
	$CpM(PH_3)H(C_2H_4)^+$	theory	10.69	

[a] Data taken from ref 11. [b] The energy of TS2 of the Co complex is taken to be the energetic maximum of the scan along the angle $\beta(M-C_a-C_b)$ in Figure 5.

However, in comparison with our best (or reference) CCSD(T)/split3 calculation, this is reproduced more closely by the MP2/4 data than by the DFT energies of these points. This result is in agreement with the literature on second-row transition-metal complexes.[63] It can also be visualized from Figure 4, which displays some key results of Table 3 in graphical form.

A global comparison between the Co, Rh, and Ir complexes shows that for the Rh and Ir complexes the agostic structure lies above the ethylene structure, but for the Co complex, the agostic structure lies below the ethylene complex. This result is in nice agreement with the experimental data of ref 9 (but for Rh, in contradiction to the DFT results of ref 3, which are included in Table 3.) An interesting feature of the Co complex is the very low energy of TS1. There is no significant barrier (below 0.4 kcal/mol) between the ethylene and agostic structures in this case and, thus, no significant activation energy for the first step of the insertion process.

A more detailed comparison between present theoretical and experimental results is provided in Table 4. The latter are taken from Brookhart et al.[11] and have been obtained for slightly

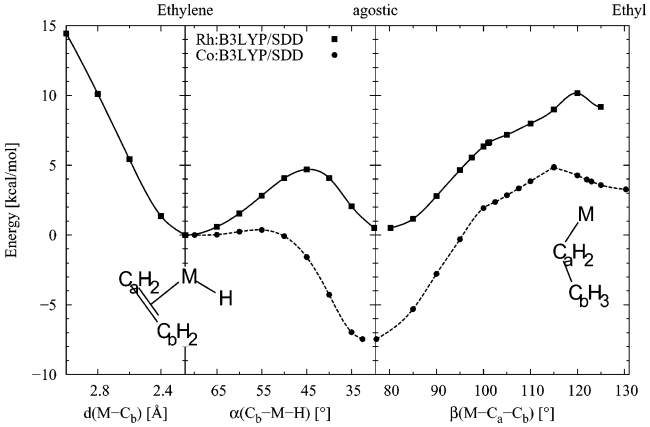

Figure 5. Coarse-grained scan (B3LYP/SDD) over approximated reaction coordinates for the Rh and Co complexes. For Co, the agostic complex is the energetic minimum which is in agreement with experiment.[9] Note the late transition state (TS2) between the agostic and ethyl structures.

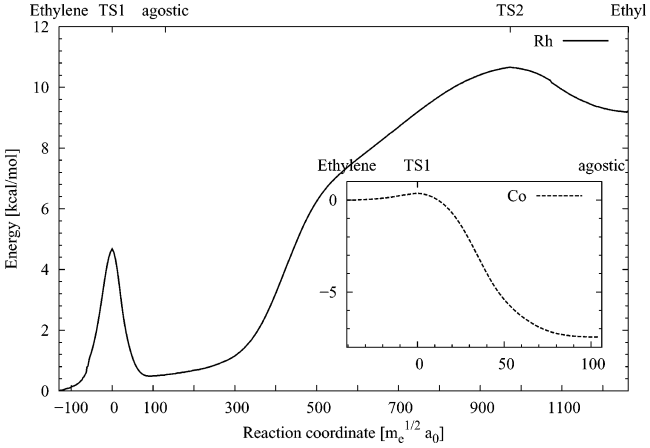

Figure 6. Reaction path in mass-weighted intrinsic coordinates (IRC). For the Rh complex, one finds a narrow first-transition barrier (TS1) and a broad second barrier (TS2) which lies energetically two times higher than the first. For the Co complex, only TS1 could be located.

different ligands as quoted in the table. Nevertheless, the agreement is quite satisfactory, especially for the Co complex, where the activation energy (difference between TS2 and agostic global minimum) is measured directly, while the energy difference to the ethylene structure is inferred indirectly (the theoretical datum of ∼12.29 kcal/mol is not from a full saddle-point optimization but estimated from the corresponding maximum of the scan in Figure 5; see also text to follow). In the case of the Rh complex, the different ligands are seen to lead to an ∼20% variation of the activation energy (energy difference between TS2 and ethylene-type global minimum). We consider it encouraging that these experimental data are between the present B3LYP result, included again in Table 4, and the high-level coupled-cluster results given in Table 3.

Motivated by this comparison, and because of the computational costs, we adhere to B3LYP/SDD as our standard computational tool for further studies. Although qualitatively MP2 fits better to high-quality reference calculations than B3LYP, the deviation may bring B3LYP into closer agreement with experiment than MP2 (by error cancellation).

3.3. Potential Energy Profiles. To solve the time-dependent Schrödinger equation, a potential energy surface (PES) is necessary. As a first approach to the treatment of the processes considered, a one-dimensional calculation has been worked out here. An approximate PES (which will be refined by an IRC calculation later in the text) has been created by a scan of the PES over two crucial reaction coordinates. The first step of the insertion process, the formation of the agostic complex from the initial ethylene structure, is described by the angle $\alpha(C_b-M-H)$. The second step, the opening of the $M-C_a-C_b$ chain which accompanies the formation of the ethyl structure, is described by the angle $\beta(M-C_a-C_b)$.

The result of the whole scan thus obtained is shown in Figure 5. All coordinates except for the respective angles are fully optimized with the B3LYP/SDD method. Because of the different reaction coordinates for the different reaction steps, the abscissa of the plot is divided into three frames with different scales. The first part of Figure 5 describes the approach of ethylene to the transition metal and the second and third panels represent the insertion process itself. Note that the last point in box two coincides with the first point in box three. The curves could not be directly connected because of the different coordinate ranges for the Rh and Co complexes.

We mention in passing that those points of the scans closest to the energy maxima (cf. Figure 5) served as initial guesses in the determination of the corresponding transition states TS1 and TS2 (in the QST3 procedure). Their nature was confirmed by establishing that there is indeed one imaginary frequency for the transition geometries. It did not prove possible to locate the TS2 of the Co complex exactly. If one takes a careful look at Figure 5, one can see that the second curve for the Co complex is not perfectly smooth at the estimated TS as it should be. This means that we move on two different pathways on the multidimensional PES. The two points to the left and right of the TS are not necessarily connected with it. Because no dynamical calculation was intended for the Co complex, this problem is, however, irrelevant for the calculations presented in the text to follow.

The scanned reaction-path profile is not appropriate for a dynamical calculation because of the different coordinates for different steps of the process. To find a reaction-path profile which reflects the whole reaction path, we calculated such a profile with the IRC method as displayed in Figure 6. This reaction coordinate shows how much two structures belonging to different points on the path differ. As anticipated from Figure 4, the three minima are indeed connected by the two transition states TS1 and TS2. The energies of the minimization procedures fit well to the curves. A new observation, extending Figure 4, is that for this complex we have a late transition state (TS2) between the agostic and ethyl structures. But for the Rh complex, we find a very narrow barrier between the ethylene and agostic structures and a very broad barrier between the agostic and ethyl structures. For the Co complex, a very low barrier between the ethylene and agostic structures is obtained. However, the nature of TS1 is confirmed by a frequency calculation. The isomerization from the ethylene structure to the agostic complex (which is the global minimum, see earlier text) should be very fast, and it should be hard to prepare the Co complex in the ethylene structure.

3.4. Wave Packet Propagation. As already pointed out, an essential part of this work consists of studying the dynamics of the insertion and, more important, of its inverse, the hydrogen elimination process, from a quantum dynamical point of view. In this way, we ultimately hope to achieve an accurate description of these elementary catalytic reaction steps including quantum features such as coherence and tunneling effects. Nevertheless, in view of the complex computational task of a multidimensional quantum calculation, we confine ourselves here, as a first step, to a one-dimensional calculation involving only the intrinsic reaction coordinate *s* (explained in Section

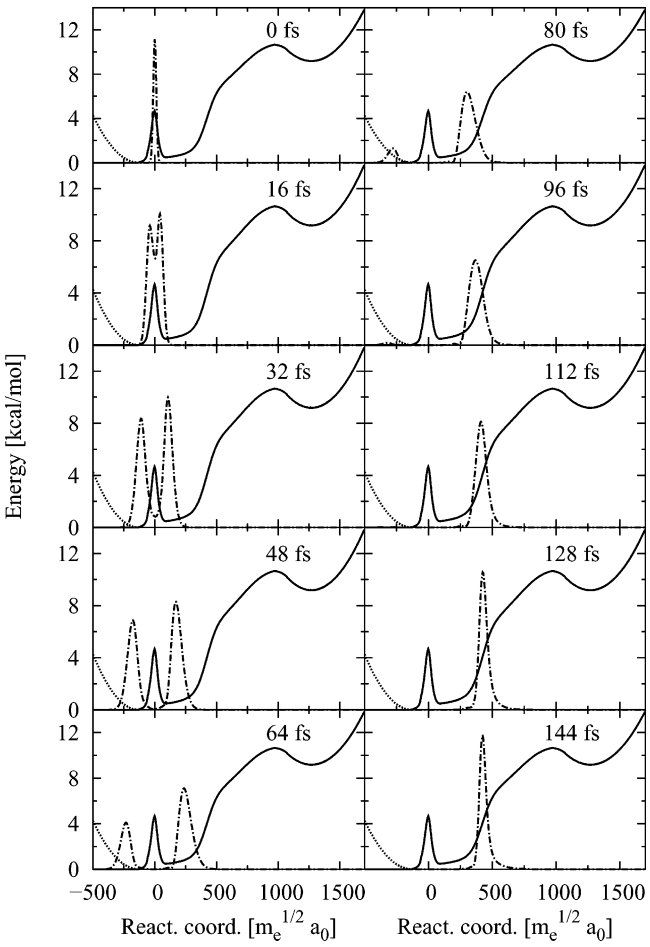

Figure 7. Snapshots of the time evolution of a wave packet starting at TS1.

2.2) by solving the time-dependent Schrödinger equation

$$\left(-\frac{\hbar^2}{2}\frac{\partial^2}{\partial s^2} + V(s)\right)\psi(s, t) = i\hbar\frac{\partial}{\partial t}\psi(s, t). \qquad (5)$$

The underlying potential energy profile $V(s)$ is that given in Figure 6. Two initial wave packets $\psi_0 = \psi(s, 0)$ are considered in the following (see also Section 2.3). They amount to a coherent excitation of the system by a fast optical transition from hypothetical neutral species with the appropriate equilibrium geometries and force constants. The simulations are thus in the spirit of the femtosecond pump probe[15] and also transition-state spectroscopy[64] and will be seen to mimic more closely the hydrogen elimination than the insertion process.

Initial Wave Packet at TS1. First, we will consider a wave packet starting at TS1. In Figure 7, the time-dependent wave function is plotted in time steps of 16 fs (dashed−dotted lines) along with the potential energy profile (full lines). The barrier around the maximum is very steep, and so, one expects fast changes of the time-dependent wave function. Indeed, already after 12 fs, the wave packet is divided into two parts, moving to the left and right sides, respectively. (Because the potential peak is not perfectly symmetric, the two parts of the wave packet are not identical.) The part on the left-hand side represents the molecules (using the statistical interpretation of the wave function) which are isomerizing to the ethylene complex. These parts are absorbed by the CAP and disappear in the drawings for later times ($t > 80$ fs).

The part which moves along the right-hand side of the barrier runs into the local minimum of the agostic structure. It evolves further into the barrier of TS2 where it is reflected (144 fs). Later times are plotted in Figure 8. After 144 fs, the wave packet runs back to the barrier of TS1 where a part of it overcomes the barrier and will be absorbed by the CAP. The rest of the packet is continuing to oscillate in the agostic minimum. During each oscillation period, a part of the wave packet is absorbed by the CAP. This process can also be studied by monitoring the norm of the time-dependent wave function in Figure 11, as will be discussed now.

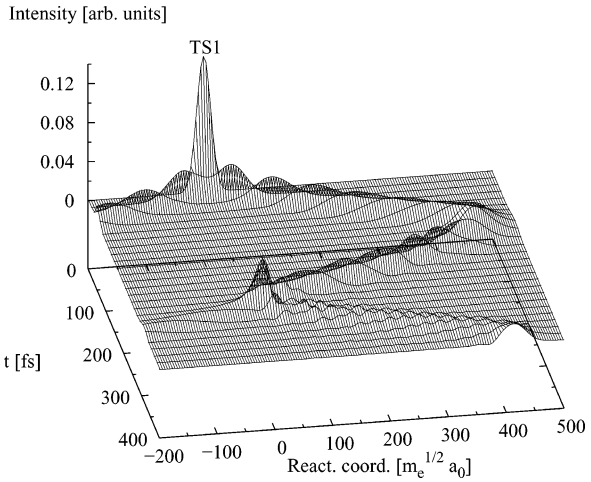

Figure 8. Oscillation of the time-dependent wave function within the agostic minimum for an initial wave packet located at TS1.

The total norm of the wave packet at the beginning of each calculation is set to one. The time-dependent norm decreases in time in steps according to Figure 11. The steps are nearly equidistant and correspond to an oscillation period of the wave packet moving in the agostic minimum of ∼260 fs. (The inspection of the time-dependent wave function in Figure 8 gives an oscillation frequency of 256 fs.) It is seen that the fractional losses of the norm are reduced for longer propagation times. This is natural, because the wave packet loses more and more energy each time it crosses the barrier.

In Figure 12, the corresponding spectrum, utilizing eqs 3 and 4, is plotted in the medium-energy regime. In the low-energy regime, the spectrum of the process where the initial wave packet starts in the agostic structure is plotted, and in the high-energy regime, the spectrum of the process where the initial wave packets start at TS2 is plotted. The latter process will be described later. The positions of the peaks are well-reproduced by filter diagonalization (vertical lines). Here, the energy difference between two states amounts to an oscillation period of ∼261 fs. This is in good agreement with the inspections of the norm (∼260 fs) and the snapshots of the time-dependent wave function (∼256 fs).

Initial Wave Packet at TS2. A qualitatively similar behavior of the time-dependent wave packet is observed, when starting at TS2 (Figure 9). Here, the initial wave packet is broader, because the coefficient of the harmonic oscillator formed by the inverted potential of this barrier is smaller. Because the potential in the central region of this reaction path is not as steep as in the case of TS1, the time evolution of the propagating wave packet is much slower. Therefore the wave packet in Figure 9 is plotted in snapshots of 32 fs in contrast to Figure 7 (where it was 16 fs). Again, one observes a bifurcation of the wave packet into two parts. One moves to the right, is reflected, and starts an oscillating process. The other part is evolving to the left into the agostic structure. Here again, one part is

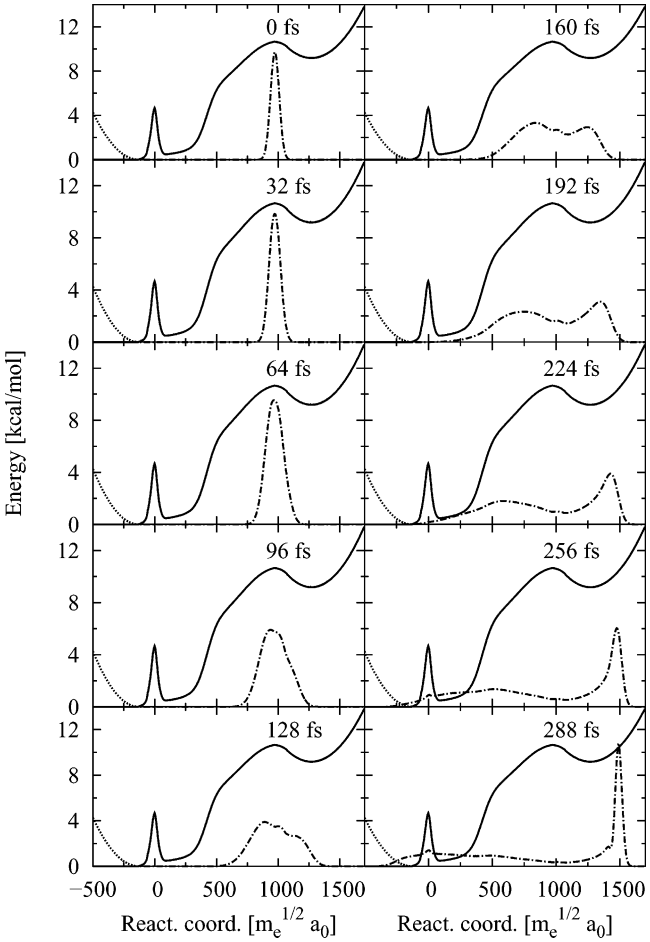

Figure 9. Snapshots of the time evolution of a wave packet starting at TS2.

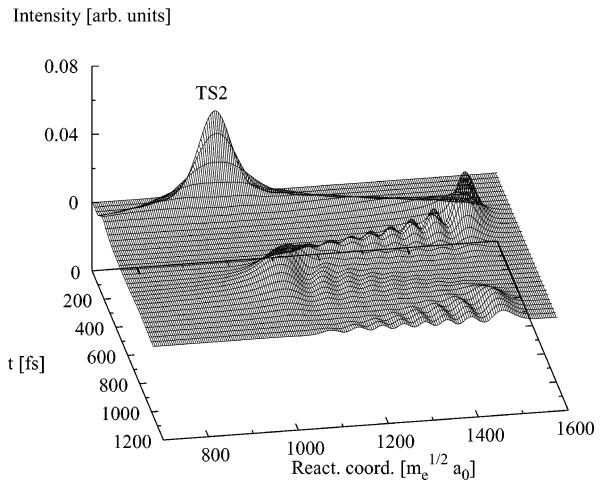

Figure 10. Oscillation of the time-dependent wave function within the ethyl minimum for an initial wave packet located at TS2.

performing an oscillation in the agostic minimum, and the other part overcomes the barrier of TS1, moves to the ethylene-type minimum, and is finally absorbed by the CAP. Thus, one finds a two-step series of oscillation, overcoming of the barrier and absorption. The oscillation frequency can also be observed by and inspecting the time-dependent norm in Figure 11. One finds a period of approximately ∼673 fs. A visual analysis of the snapshots in Figure 10 gives ∼672 fs; a measurement at the spectrum (which should be the most accurate value) gives ∼689 fs. If the Rh complex could be prepared in TS2, Figure 11 shows that the isomerization to the ethylenic ground-state goes much

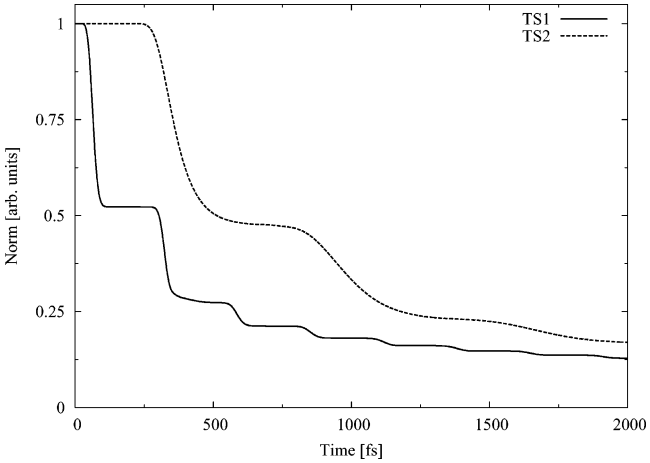

Figure 11. Time evolution of the norm of a wave packet starting at TS1 and TS2. The steps can be assigned to the absorption of the wave function through the CAP and thus to the oscillation frequency of the packet within a minimum of the potential.

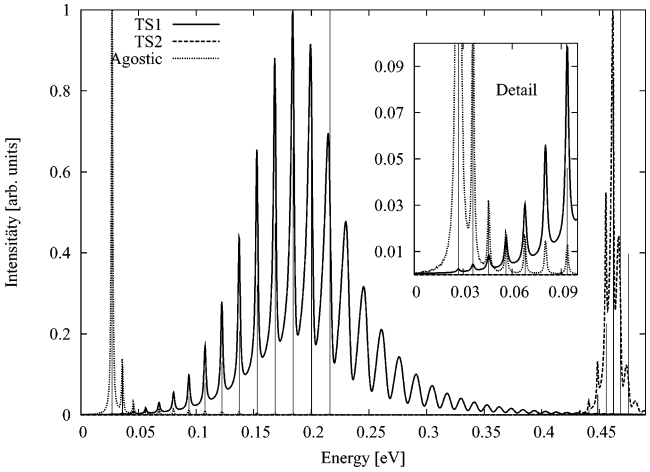

Figure 12. Calculated spectra of isomerization processes where the initial wave packet is located at TS1, TS2, and the agostic structure. The vertical lines are calculated with filter diagonalization. The inset shows the overlap between the TS1 and the agostic spectrum.

more slowly than for TS1. The time delay (half norm) of the TS2 isomerization is ∼300 fs.

Initial Wave Packet at the Agostic Minimum. The left-hand side of Figure 12 and the inset show what happens if a wave packet is started in the agostic minimum. The energy levels of the tail of this spectrum overlap perfectly with those of the TS1 spectrum (see insert), which is a good test for the reliability of the spectral calculations. The energy eigenvalues are the same. However, this starting position gives no interesting dynamics, because the wave packet stays in the minimum. The time-dependent wave function broadens and contracts slightly during the time evolution, because its width is not adapted to the curvature of the potential. The quasi-stationary evolution of the wave packet leads to the sharp spectrum for this process.

4. Summary and Outlook

The $[CpM(PH_3)H(C_2H_4)]^+$, (M = Rh, Co), complexes have been investigated theoretically by electronic structure and quantum dynamical methods. Stationary points including transition points have been found with various methods and basis sets. The geometries and energies have been described in detail. A one-dimensional reaction-path profile has been calculated for the Rh complex and has been used for wave packet propagation treatment of the dynamics.

In combination with earlier work on the analogous Ir complex,[23,65] the geometrical data for one transition-metal triad is now established and available. As expected, a two-step process for the insertion for all three transition-metal complexes is obtained. The influence of the correlation methods and the basis sets on the geometries is rather weak. The Co complex differs structurally and energetically from the Rh and Ir cases. The latter two species show no systematic differences in their bond distances or angles.

Accurate CCSD(T) calculations allow a detailed comparison between various DFT functionals and also MP2. For the Rh complex, it is found that MP2 is closer to the CCSD(T) results than B3LYP. This has also been found (and rationalized) for other second-row transition metals.[63] BP86 gives better energies and is also faster than B3LYP. Its influence on the calculated geometries is rather small. The agostic structure seems to play a special role in this context, because here, we observe the largest deviations. The agostic structure turns out to be the ground state for the Co complex. This is in agreement with the experiment. There is no significant barrier between the ethylene and agostic structures for the Co complex (for B3LYP/SDD, below 0.4 kcal/mol).

The reaction-path profile shows for the Rh complex a late transition state between the agostic and ethyl complexes. This barrier, as calculated by the B3LYP/SDD method, is high (∼10.7 kcal/mol) and broad, in contrast to the barrier between the ethylene and agostic complexes (∼4.7 kcal/mol). This indicates a complicated PES in many dimensions. The wave packet propagations performed are novel and represent a first attempt to treat the dynamics of these systems from a quantal point of view. They simulate an experimental preparation of the complex in one of the two transition-state structures and its isomerization toward the ethylene complex. The speed of the isomerization depends strongly on the position of the initial wave packet on the reaction-path potential. Two oscillation periods of ∼260 fs (when starting at TS1) and ∼690 fs (when starting at TS2) have been obtained from the spectrum. These correspond to the oscillations of the wave packets in the agostic and ethyl structures, respectively. The preliminary lifetimes for the complexes prepared in one of the transition states are in the subpicosecond range (see Figure 11) and apparently amount to an extremely fast β-hydrogen elimination under the nonequilibrium conditions in question. However, because of the restriction to one degree of freedom only, the result is to be considered only preliminary.

The next series of dynamical calculations should incorporate more degrees of freedom. For this purpose, a kinetic energy operator is currently in preparation and an appropriate potential energy surface will be calculated. To speed up this calculation, a locally harmonic expansion of the energy surface around the minimum energy path may be used (at least for some degrees of freedom). We emphasize that important parts of the anharmonicity are still retained, because the expansion parameters depend on the other coordinates. Correspondingly, the vinylidene−acetylene isomerization has been treated and could be described very well by such an approach.[66] A more realistic treatment of the ligands is also optional for future work. In this way, we hope to achieve more insight into the factors governing the structural and dynamical features of these transition-metal complexes.

Acknowledgment. The authors gratefully acknowledge helpful discussions with Hubert Wadepohl and Ute Kohl. This work has been supported financially by the *Deutsche Forschungsgemeinschaft* through *Sonderforschungsbereich 623* "Molekulare Katalysatoren: Struktur und Funktionsdesign".

References and Notes

(1) Koga, K.; Morokuma, K. *Chem. Rev.* **1991**, *91*, 823.
(2) Musaev, D. G.; Morokuma, K. *Adv. Chem. Phys.* **1996**, *95*, 61.
(3) Ziegler, T. *Chem. Rev.* **1991**, *91*, 651.
(4) Salahub, D. R.; Castro, M.; Fournier, R.; Calaminici, P.; Godbout, N.; Goursot, A.; Jamorski, C.; Kobayashi, H.; Martinez, A.; Papai, I.; Proynow, E.; Russo, N.; Sirois, S.; Ushio, J.; Vela, A. In *Theoretical and computational approaches to interface phenomena*; Sellers, H., Olab, J., Eds.; Plenum Press: New York, 1995; p 817.
(5) Siegbahn, P. E. M. *Adv. Chem. Phys.* **1996**, *93*, 333.
(6) *Transition metal hydrides*; Dedieu, A., Ed.; VCH Publishers: New York, 1992.
(7) *Theoretical aspects of homogeneous catalysts. Applications of ab initio molecular orbital theory*; van Leeuwen, P. W., van Lenthe, J. H., Morokuma, K., Eds.; The Netherlands, 1994.
(8) Yoshida, S.; Sakaki, S.; Kobayashi, H. *Electronic processes in catalysis*; VCH Publishers: New York, 1992.
(9) Brookhart, M.; Green, M. L. H.; Wong, L.-L. *Prog. Inorg. Chem.* **1988**, *36*, 1.
(10) Brookhart, M.; Lincoln, D. M.; Volpe, A. F.; Schmidt, G. F. *Organometallics* **1989**, *8*, 1212.
(11) Brookhart, M.; Hauptman, E.; Lincoln, D. M. *J. Am. Chem. Soc.* **1992**, *114*, 10394.
(12) Ittel, S. D.; Johnson, L. K.; Brookhart, M. *Chem. Rev.* **2000**, *100*, 1169.
(13) Senn, H. M.; Blöchel, P.; Togni, A. *J. Am. Chem. Soc.* **2000**, *122*, 4098.
(14) Meier, R. J.; van Doremaele, G. H.; Ialori, S.; Buda, F. *J. Am. Chem. Soc.* **1994**, *116*, 7274.
(15) Zewail, A. H. Atomic-scale dynamics of the chemical bond using ultrafast lasers. Nobel Lecture, 1999.
(16) Zewail, A. H. *Femtochemistry*; World Scientific: Singapore, 1994; Vols. 1 and 2.
(17) Manz, J.; Wöste, L. *Femtosecond Chemistry*; Verlag Chemie: Weinheim, Germany, 1995.
(18) Schork, R.; Köppel, H. *J. Chem. Phys.* **2001**, *115*, 7907.
(19) Mahapatra, S.; Köppel, H.; Cederbaum, L. S. *J. Phys. Chem.* **2001**, *105*, 2321.
(20) Somers, M. F.; Kingma, S. M.; Pijper, E.; Kroes, G. J.; Lemoine, D. *Chem. Phys. Lett.* **2002**, *360*, 390.
(21) Kulander, K. C. *Time-dependent methods for quantum dynamics;* North-Holland, 1991.
(22) Zhang, J. Z. *Theory and application of quantum molecular dynamics*; World Scientific: River Edge, NJ, 1999.
(23) Niu, S.; Zaric, S.; Bayse, C. A.; Strout, D. L.; Hall, M. B. *Organometallics* **1998**, *17*, 5139.
(24) Parr, R. G.; Lee, W. *Density-functional theory of atoms and molecules*; Oxford University Press: New York, 1989.
(25) Becke, A. D. *Phys. Rev. A* **1988**, *38*, 3098.
(26) Perdew, J. P. *Phys. Rev. B* **1986**, *33*, 8822.
(27) Becke, A. D. *J. Chem. Phys.* **1993**, *98*, 1372.
(28) Becke, A. D. *J. Chem. Phys.* **1993**, *98*, 5648.
(29) Møller, C.; Plesset, M. S. *Phys. Rev.* **1936**, *46*, 618.
(30) Pople, J. A.; Binkley, J. S.; Seeger, R. *Int. J. Quantum Chem., Quantum Chem. Symp.* **1976**, *10*, 1.
(31) Krishnan, R.; Pople, J. A. *Int. J. Quantum Chem., Quantum Chem. Symp.* **1978**, *14*, 91.
(32) Cizek, J. *Adv. Chem. Phys.* **1969**, *14*, 35.
(33) Purvis, G. D., III; Bartlett, R. J. *J. Chem. Phys.* **1982**, *76*, 1910.
(34) Scuseria, G. E.; Janssen, C. L.; Schaefer, H. F., III *J. Chem. Phys.* **1988**, *89*, 7382.
(35) Dunning, T. H., Jr.; Hay, P. J. In *Modern Theoretical Chemistry*; Schaefer H. F., III, Ed.; Plenum: New York, 1976; Vol. 3, p 1.
(36) Ditchfield, R.; Hehre, W. J.; Pople, J. A. *J. Chem. Phys.* **1971**, *54*, 724.
(37) Hehre, W. J.; Ditchfield, R.; Pople, J. A. *J. Chem. Phys.* **1972**, *56*, 2257.
(38) Hariharan, P. C.; Pople, J. A. *Mol. Phys.* **1974**, *27*, 209.
(39) Frisch, M. J.; Trucks, G. W.; Schlegel, H. B.; Scuseria, G. E.; Robb, M. A.; Cheeseman, J. R.; Zakrzewski, V. G.; Montgomery, J. A., Jr.; Stratmann, R. E.; Burant, J. C.; Dapprich, S.; Millam, J. M.; Daniels, A. D.; Kudin, K. N.; Strain, M. C.; Farkas, O.; Tomasi, J.; Barone, V.; Cossi, M.; Cammi, R.; Mennucci, B.; Pomelli, C.; Adamo, C.; Clifford, S.; Ochterski, J.; Petersson, G. A.; Ayala, P. Y.; Cui, Q.; Morokuma, K.; Malick, D. K.; Rabuck, A. D.; Raghavachari, K.; Foresman, J. B.; Cioslowski, J.; Ortiz, J. V.; Stefanov, B. B.; Liu, G.; Liashenko, A.; Piskorz, P.; Komaromi, I.; Gomperts, R.; Martin, R. L.; Fox, D. J.; Keith, T.; Al-Laham, M. A.; Peng, C. Y.; Nanayakkara, A.; Gonzalez, C.; Challacombe, M.; Gill, P. M.

W.; Johnson, B. G.; Chen, W.; Wong, M. W.; Andres, J. L.; Head-Gordon, M.; Replogle, E. S.; Pople, J. A. *Gaussian 98*; Gaussian, Inc.: Pittsburgh, PA, 1998.
(40) Fukui, K.; Sato, S.; Fujimoto, H. *J. Am. Chem. Soc.* **1975**, *97*, 1.
(41) Fukui, K. *Acc. Chem. Res.* **1981**, *14*, 363.
(42) Gonzalez, C.; Schlegel, H. B. *J. Chem. Phys.* **1989**, *90*, 2154.
(43) Gonzalez, C.; Schlegel, H. B. *J. Phys. Chem.* **1990**, *94*, 5523.
(44) Peng, C.; Schlegel, H. B. *Isr. J. Chem.* **1993**, *33*, 449.
(45) Arnoldi, W. E. *Q. Appl. Math.* **1951**, *9*, 17.
(46) Saad, Y. *Lin. Alg. Appl.* **1980**, *24*, 269.
(47) Park, T. J.; Light, J. C. *J. Chem. Phys.* **1986**, *85*, 5870.
(48) Balakrishnan, N.; Kalyanaraman, C.; Sathyamurthy, N. *Phys. Rep.* **1997**, *280*, 79.
(49) Kosloff, R. In *Dynamics of Molecules and Chemical Reactions*; Wyatt, R. E., Zhang, J. Z., Eds.; Marcel Dekker: New York, 1996; p 185.
(50) Sorensen, H. V.; Burrus, C. S.; Heideman, M. T. *Fast Fourier Transform Database*; PWS Publishing: 1995.
(51) McClellan, J. H.; Rader, C. M. *Number Theory in Digital Signal Processing*; Prentice-Hall: Englewood Cliffs, NJ, 1979.
(52) Nussbaumer, H. J. *Fast Fourier Transform and Convolution Algorithms*; Springer-Verlag: New York, 1982.
(53) Neuhauser, D.; Baer, M. *J. Chem. Phys.* **1989**, *90*, 4351.
(54) Vibók, Á.; Balint-Kurti, G. G. *J. Chem. Phys.* **1992**, *96*, 7615.
(55) Vibók, Á.; Balint-Kurti, G. G. *J. Phys. Chem.* **1992**, *96*, 8712.
(56) Riss, U. V.; Meyer, H.-D. *J. Chem. Phys.* **1996**, *105*, 1409.
(57) Schinke, R. *Photodissociation dynamics*; Cambridge University Press: Cambridge, 1993.
(58) Neuhauser, D. *J. Chem. Phys.* **1990**, *93*, 2611.
(59) Neuhauser, D. *J. Chem. Phys.* **1993**, *100*, 5076.
(60) Wall, M. R.; Neuhauser, D. *J. Chem. Phys.* **1995**, *102*, 8011.
(61) Mandelshtam, V. A.; Taylor, H. S. *J. Chem. Phys.* **1997**, *107*, 6756.
(62) Helgaker, T.; Jørgensen, P.; Olsen, J. *Molecular electronic-structure theory*; John Wiley & Sons: New York, 2000.
(63) Niu, S.; Hall, M. B. *Chem. Rev.* **2000**, *100*, 353.
(64) Metz, R. B.; Bradforth, S. E.; Neumark, D. M. *Adv. Chem. Phys.* **1992**, *81*, 1.
(65) Han, Y.; Deng, L.; Ziegler, T. *J. Am. Chem. Soc.* **1997**, *119*, 5939.
(66) Bittner, M.; Köppel, H. *Phys. Chem. Chem. Phys.* **2003**, *5*, 4604.